APL Photonics

Tuning intrinsic photoluminescence from light-emitting multispectral nanoporous anodic alumina photonic crystals

Cite as: APL Photonics **7**, 026108 (2022); https://doi.org/10.1063/5.0078505
Submitted: 13 November 2021 • Accepted: 31 January 2022 • Accepted Manuscript Online: 31 January 2022 • Published Online: 25 February 2022

Laura K. Acosta, Cheryl Suwen Law, Abel Santos, et al.

Tuning intrinsic photoluminescence from light-emitting multispectral nanoporous anodic alumina photonic crystals

Cite as: APL Photon. 7, 026108 (2022); doi: 10.1063/5.0078505
Submitted: 13 November 2021 • Accepted: 31 January 2022 •
Published Online: 25 February 2022

View Online Export Citation CrossMark

Laura K. Acosta,[1] Cheryl Suwen Law,[2,3,4] Abel Santos,[2,3,4] Josep Ferré-Borrull,[1] and Lluis F. Marsal[1,a)]

AFFILIATIONS

[1] Department of Electronic, Electric, and Automatics Engineering, Rovira i Virgili University, Tarragona 43007, Spain
[2] School of Chemical Engineering and Advanced Materials, The University of Adelaide, Adelaide, South Australia 5005, Australia
[3] Institute for Photonics and Advanced Sensing, The University of Adelaide, Adelaide, South Australia 5005, Australia
[4] ARC Centre of Excellence for Nanoscale BioPhotonics, The University of Adelaide, Adelaide, South Australia 5005, Australia

[a)] Author to whom correspondence should be addressed: lluis.marsal@urv.cat

ABSTRACT

To control and harness the intrinsic photoluminescence of solid-state, light-emitting materials produced by self-organization approaches remain challenging. This study demonstrates how the intrinsic broadband photoluminescence emission from nanoporous anodic alumina (NAA) produced by anodization of aluminum in oxalic acid electrolyte can be precisely tuned by engineering its structure in the form of photonic crystals (PCs). A combination of pulse and constant anodization in distinct acid electrolytes makes it possible to engineer a novel heterogeneous optical structure consisting of two layers: (i) a non-emitting, light-filtering layer in the form of multi-spectral nanoporous anodic alumina photonic crystals (MS–NAA–PCs) on its top (i.e., 58 μm thick and average pore diameter of 17 nm) and (ii) an intrinsically light-emitting layer of NAA at its bottom (i.e., 50 μm thick an average pore diameter of 40 nm). MS–NAA–PCs are engineered to feature three intense, well-resolved photonic stopbands (PSBs), the positions of which are spaced at specific regions of the visible spectrum from ~380 to 560 nm. It is demonstrated that the PSBs of the non-emitting MS–NAA–PCs on top of the heterogeneous optical structure act as a light-filtering component, which makes it possible to narrow and tune the characteristically broad, Gaussian-like photoluminescence emission from the underlying light-emitting NAA layer. This structural design makes it possible to narrow the width of photoluminescence emission up to ~50 nm and blue shift its position for ~15 nm. Our advances pave the way for novel designs of intrinsic, light-emitting NAA-based PC structures, which could find broad applicability across light technologies, such as sensing and biosensing, photodetection, and solar light harvesting.

I. INTRODUCTION

Solid-state light-driven luminescence—henceforth "photoluminescence" or PL—is a class of light–matter interaction in which incident photons absorbed by a material's atoms excite electrons to higher energy levels. Once excited, electrons undergo certain relaxation processes through which photons are re-radiated or emitted in the form of a light beam.[1] The properties of the emitted photoluminescent beam rely on the electronic band structure of the photo-excited material.[2] Characteristically, PL emissions from solid-state materials with defects in their electronic band structure are spectrally broad, featuring a Gaussian-like emission centered within the vicinity of the exciton resonance—typically at a longer wavelength than that of the excitation input.[3] Broad PL emissions can be narrowed by distinct strategies to fulfill requirements for specific applications, such as lasing,[4] LEDs,[5,6] bioimaging,[7] and diagnostics and sensing.[8,9] Of all these, engineering the structure of light-emitting materials at the nanoscale in the form of photonic crystals (PCs) enables highly directional emission of light with tunable wavelength by confining, enhancing, and

attenuating emitted light at specific, narrow spectral regions.[10,11] PCs are optical structures with allowed and forbidden photonic stopbands (PSBs) that modify the group velocity of incident or emitted photons when these flow through the PCs' structure. Light–matter interactions in PCs can be tuned with precision by engineering their architecture so that regions with high and low refractive indices are periodically and spatially distributed following specific patterns.[12] A variety of PC forms based on a broad range of materials can be produced to control electromagnetic waves with versatility over the broad spectrum from UV to IR. Currently, PCs have multiple applications, including chemical sensing and biosensing,[13–18] photonic encoding,[19] lasing,[20–25] and photocatalysis.[26,27] Nanoporous PCs are particularly suitable platform materials to tailor photo-induced light emissions both extrinsically and intrinsically. In the former mode, a host non-photoluminescent nanoporous PC is infiltrated with a photoluminescent material to enhance, filter, or guide its light emission,[27] while in the latter configuration, a photoluminescent nanoporous PC material filters its own PL emission.[28] Nanoporous anodic alumina (NAA) has long been devised as an ideal nanoporous PC platform material due to its cylindrical nanopores with well-defined and highly controllable geometric features.[29–32] NAA is produced by electrochemical oxidation—anodization—of aluminum, which is a cost-effective and fully scalable top–down industrial process compatible with conventional micro- and nanofabrication. Although architecture, dimensions, and distribution of nanopores in NAA can be precisely engineered in a variety of NAA-based PCs (NAA–PCs) during anodization,[33–35] its intrinsic optical properties—refractive index and photoluminescence—are critically determined by the anodizing acid electrolyte, anodization regime, and post-anodization treatments, such as annealing.[36] The origin of PL in NAA is thought to be attributable to two types of photoluminescent centers: (i) F^+ centers[37–39] related to ionized oxygen vacancies and (ii) F^- centers associated with carboxylate impurities incorporated from the acid electrolyte during anodization.[40,41] The position and intensity of NAA's PL emission depend intrinsically on the quantity of F^+ and F^- centers and their respective distribution across the structure of NAA. NAA films produced in oxalic acid feature more intense PL emission than that of its counterparts fabricated in sulfuric or phosphoric acids.[42–46] NAA's PL intensity also decreases with annealing temperature due to the elimination of oxygen vacancies and impurities in its structure through crystallographic organization and burning under oxygen atmosphere.[47–52] Pioneering studies on 2D NAA–PCs featuring straight nanopores demonstrated their application as host materials to tune PL emissions from fluorescent dyes infiltrated in their nanoporous matrix.[57,58] In this system, the red edge of the characteristic photonic stopband (PSB) of NAA–PCs reduces the group velocity of incident photons at that spectral region by the so-called "slow photon" effect. As a result, PL emission is enhanced due to increasing frequency of interactions between exciting photons and light-emitting molecules at that spectral region—increase in the radiative rate.[25] An alternative approach would be to tailor the intrinsic photoluminescence of NAA by engineering its structure in the form NAA–PCs.[53,54] Under this configuration, alignment of the NAA–PC's PSB with the Gaussian-like PL emission of NAA would narrow its linewidth by internally forbidding light propagation at specific spectral regions. Surprisingly, to the best of our knowledge, this system has not been explored yet.

In this work, we demonstrate for the first time how the intrinsic photoluminescence of NAA can be tuned by engineering its structure in the form of multispectral PCs (MS–NAA–PCs)—NAA–PCs featuring multiple PSBs at specific spectral positions (see Fig. 1). Spectral alignment between the three characteristic PSBs of MS–NAA–PCs and the photoluminescence emission of NAA [see Fig. 1(a)] makes it possible to judiciously narrow its linewidth with precision by inhibiting light propagation at specific spectral positions [see Fig. 1(b)]. Our results create exciting new opportunities to modulate light emission from NAA-based structures, which could have broad implications across optoelectronic disciplines, such as lasing, sensing, energy harvesting, and photocatalysis.

II. EXPERIMENTAL

A. Materials

High purity aluminum circular chips (Al) (0.5 mm thickness and 99.99% purity) were acquired from Goodfellow Cambridge Ltd. (UK). Acetone [$(CH_3)_2CO$], ethanol (EtOH; C_2H_5OH), perchloric acid ($HClO_4$), oxalic acid ($H_2C_2O_4$), hydrochloric acid (HCl), sulfuric acid (H_2SO_4), chromic acid (H_2CrO_4), phosphoric acid (H_3PO_4), and copper chloride ($CuCl_2$) were provided by Sigma-Aldrich (Spain). Double deionized water (DI) (18.2 MΩ cm) was used to prepare all aqueous solutions, unless otherwise specified.

B. Fabrication of reference NAA films

A set of NAA films featuring straight cylindrical nanopores from the top to the bottom were used as a reference material to quantify bulk PL emission. Al disks were anodized by the two-step process, full details of which are reported elsewhere.[52–56] Briefly, before anodization, Al chips were electropolished in a mixture of EtOH and $HClO_4$ 4:1 (v:v) at 20 V and 5 °C for 3 min. Then, the first anodization step was carried out in 0.3M $H_2C_2O_4$ aqueous electrolyte at 40 V and 5 °C for 20 h. Next, the resulting NAA layer was selectively removed by wet chemical etching in a mixture of 0.2M H_2CrO_4 and 0.4M H_3PO_4 for 3 h at 70 °C. After this, the second anodization step was performed under the same anodization conditions for a total charge density (integrated current density throughout time per unit of area) of 113.2 C cm^{-2} under voltage control conditions at 40 V to generate a NAA film of ~50 μm featuring straight cylindrical nanopores.

C. Fabrication of MS–NAA–PCs

Fabrication of MS–NAA–PCs was performed following a modified two-step anodization process. Electropolished Al chips were first anodized in a 0.3M sulfuric acid electrolyte at 5 °C under constant voltage at 25 V for 20 h. The NAA film was then chemically dissolved in a mixture of 0.2M H_2CrO_4 and 0.4M H_3PO_4 for 3 h at 70 °C. Then, a 10-min second step in the same acid electrolyte at 25 V for 10 min was applied to generate a shuttle layer for homogeneous nanopore growth. Then, the anodization process was switched to sinusoidal pulse anodization under current density control conditions. During this process, a sinusoidal current density input profile was applied to modulate the nanopore diameter in depth and generate gradient-index filter PC structures.[59] MS–NAA–PCs consisted of

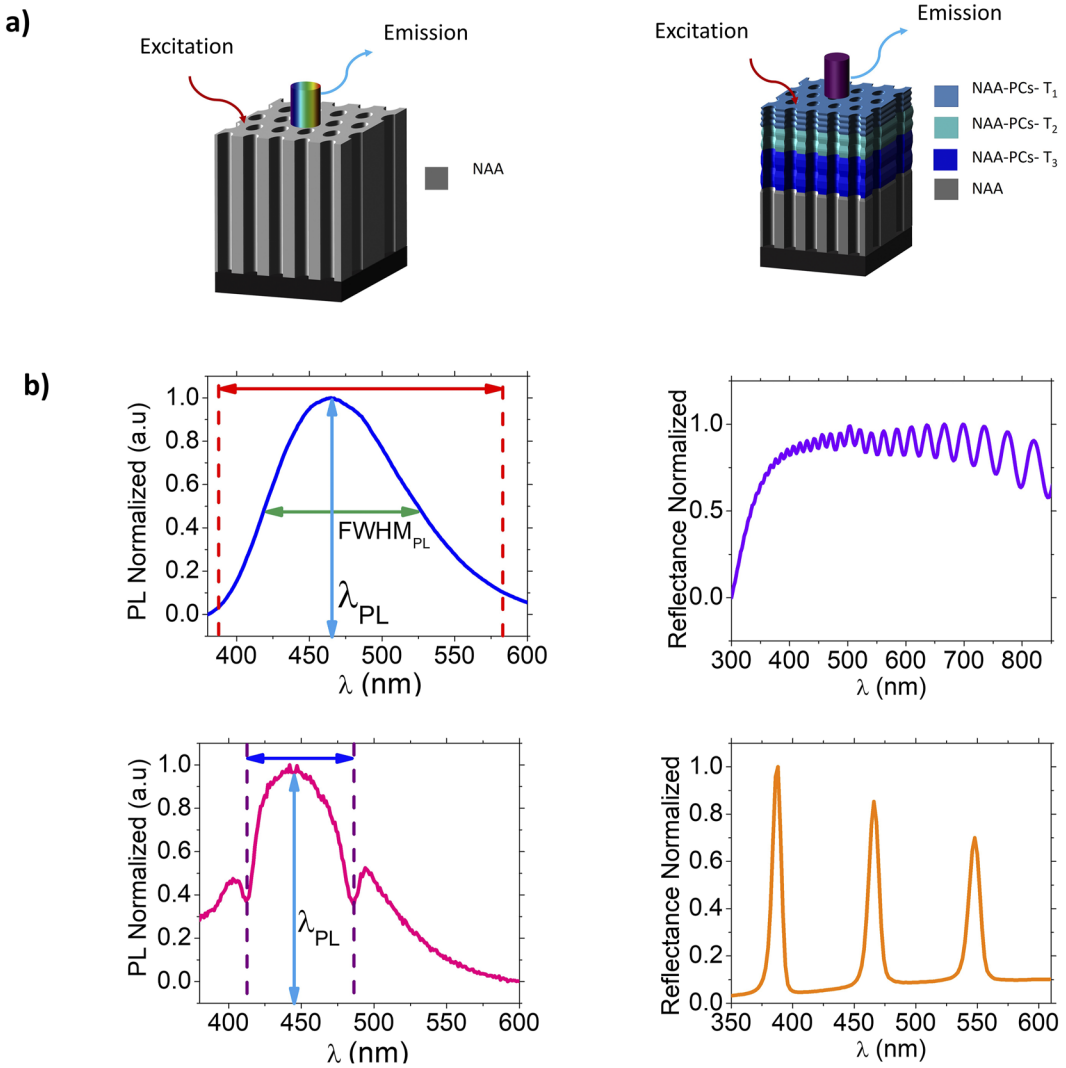

FIG. 1. Conceptual illustration showing the mechanism by which MS–NAA–PCs narrow PL emission from NAA by judicious alignment of PSBs. (a) Schematic showing the PL emission of a reference NAA (left) and a MS–NAA–PC (right). (b) Normalized reflection and PL spectra of a NAA film (top) and a MS–NAA–PC (bottom) showing the mechanism by which PSBs in MS–NAA–PCs are harnessed to selectively filter PL emission from NAA, where λ_{PL} and $FWHM_{PL}$ represent the central wavelength position and full width at half maximum of the PL emission of NAA and MS–NAA–PCs, respectively.

a NAA layer featuring three gradient-index filters generated by judiciously modulating the anodizing current density waveform input into sequential sinusoids with three different pulse periods (i.e., T_1, T_2, and T_3), as described by the following equation:

$$J(t) = \begin{cases} \mathrm{J_1}\ \sin\left(\dfrac{2\pi}{\mathrm{T_1}}t\right) + \mathrm{J_0}, & 0 \le t < N\mathrm{T_1}, \\ \mathrm{J_1}\ \sin\left(\dfrac{2\pi}{\mathrm{T_2}}t\right) + \mathrm{J_0}, & N\mathrm{T_1} \le t < N\mathrm{T_1} + N\mathrm{T_2}, \\ \mathrm{J_1}\ \sin\left(\dfrac{2\pi}{\mathrm{T_3}}t\right) + \mathrm{J_0}, & N\mathrm{T_1} + N\mathrm{T_2} \le t < N\mathrm{T_1} + N\mathrm{T_2} + N\mathrm{T_3}, \end{cases} \quad (1)$$

where $J(t)$ is the anodization current density at time t (in seconds), J_1 is the current density amplitude (in mA cm^{-2}), T_i (i = 1, 2, 3) is the anodization period i (in seconds), and J_0 is the offset current density (in mA cm^{-2}). The offset current density (J_0), current density amplitude (J_1), and number of periods (N) were kept constant throughout the anodization process for all MS–NAA–PCs fabricated in this study, while the anodization periods were varied as T_1 = 125 s, T_2 = 150 s, and T_3 = 175 s for N = 100 pulses per period (N_1, N_2, and N_3) (i.e., total of 300 pulses). After this, a 50 μm thick NAA layer produced in 0.3, M oxalic electrolyte (i.e., light-emitting layer) was generated under potentiostatic conditions at 40 V (i.e., third anodization step). Table I summarizes the fabrication conditions used to fabricate MS–NAA–PCs. After anodization, the aluminum

TABLE I. Fabrication conditions of MS–NAA–PCs, including current density amplitude (J_1), anodization period (T_i), and offset current density (J_0).

	J_0 (mA cm^{-2})	J_1 (mA cm^{-2})	T_1 (s)	T_2 (s)	T_3 (s)	N_1 (pulses)	N_2 (pulses)	N_3 (pulses)
MS-NAA-PCs	1.98	1.41	125	150	175	100	100	100

substrate remaining at the backside of MS–NAA–PCs was removed by selective chemical etching in a saturated solution of HCl and $CuCl_2$ for optical characterization.

D. Optical characterization of MS-NAA-PCs

Reflection spectra from MS–NAA–PCs were measured from 250 to 900 nm with a resolution of 2 nm at varying angle of incidence from 8° to 65° in a PerkinElmer UV–visible–NIR Lambda 950 spectrophotometer. The reflection intensity (R_{PSB}), position of central wavelength (λ_{PSB}), and full width at half maximum ($FWHM_{PSB}$) of the photonic stopbands (PSBs) of MS–NAA–PCs were estimated from reflection spectra through Gaussian fittings performed in OriginPro8.5®. PL spectra from MS–NAA–PCs were acquired in a fluorescence spectrophotometer (Photon Technology International Inc., Division of Horiba, USA) equipped with a Xe lamp as an excitation light source at room temperature and at an excitation wavelength (λ_{ex}) of 355 nm. PL measurements were performed from the top side of reference NAA films and MS–NAA–PCs using a commercial bandpass filter with a cutoff wavelength of 350 nm.

E. Structural characterization of MS-NAA-PCs

Morphological and structural features of NAA films and MS–NAA–PCs were characterized by a field-emission gun scanning electron microscope (FEG-SEM FEI Quanta 450) operating at an accelerating voltage of 20–25 keV. Characteristic geometric features of MS–NAA–PCs were quantified by analyzing FEG-SEM images in ImageJ software.[60]

III. RESULTS AND DISCUSSION

A. Fabrication and structural characterization of MS-NAA-PCs

Figure 2(a) illustrates the fabrication process used to produce the light-filtering layer of MS–NAA–PCs under sinusoidal current density conditions, including a full-view of a representative anodization profile. Figure 2(b) shows magnified views of this sinusoidal pulse anodization process in which the current density period (T_i)—time between consecutive sinusoidal pulses—is increased from 125 to 175 s with a step size ΔTi = 25 s after each 100 pulses. This input current density profile results in three stacked

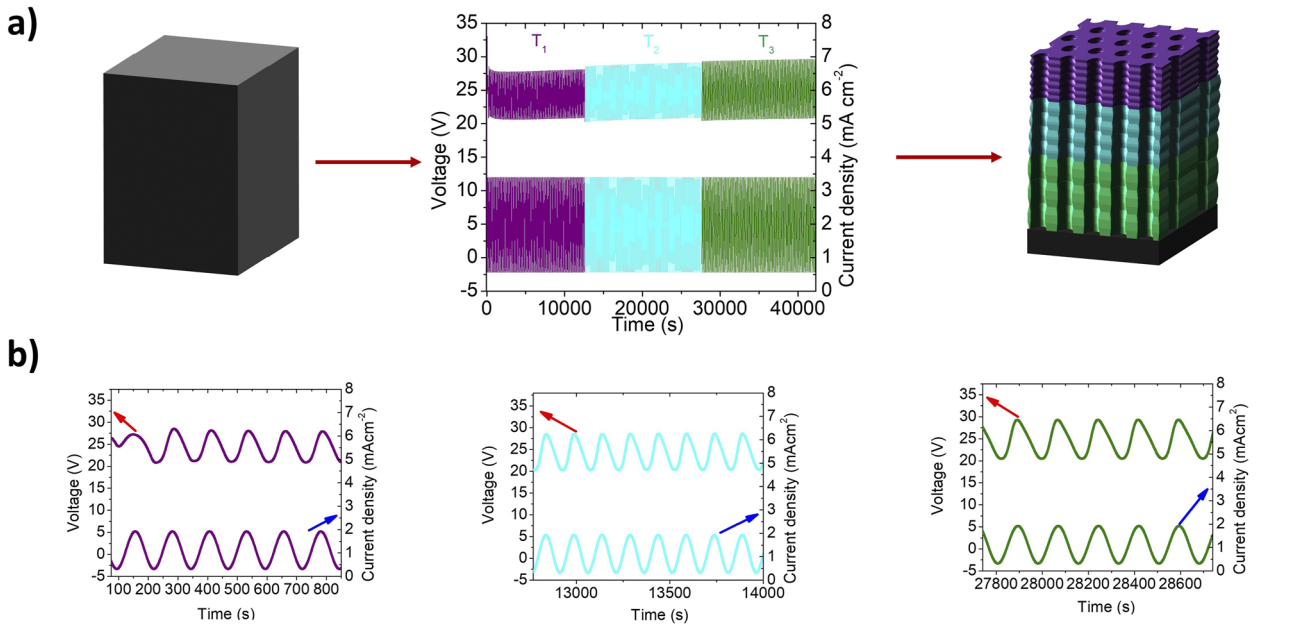

FIG. 2. Fabrication of MS–NAA–PCs by sinusoidal pulse anodization. (a) Schematics of the fabrication process to produce MS–NAA–PCs by a sinusoidal current density profile with three anodization periods (T_1, T_2, and T_3), including aluminum substrate (left), representative full-view anodization profile with the current density input and voltage output (center), and resulting MS–NAA–PC featuring three stacked gradient-index filters (right). (b) Magnified views of the sinusoidal current density profile shown in (a) for each anodization period (T_1, T_2, and T_3) demonstrating the precise translation of current density pulses into sinusoidal voltage output pulses.

layers of NAA featuring a modulated nanopore diameter in depth, each of which represents a gradient-index filter with its characteristic PSB. As such, the optical response of the composite NAA–PC features three PSBs, one for each NAA gradient-index filter composing the overall PC structure. It is apparent from these graphs that under the fabrication conditions used in our study, the sinusoidal current density input with $J_0 = 1.98$ mA cm^{-2}, $J_1 = 1.41$ mA cm^{-2}, $T_1 = 125$ s, $T_2 = 150$ s, and $T_3 = 175$ s for a total of 300 pulses is precisely translated into a sinusoidal voltage output, which mimics the frequency of the input profile. Analysis of this anodization profile indicates that the amplitude of the sinusoidal voltage output slightly increases with increasing T_i from ~20–25 V at $T_1 = 125$ s to ~20–29 V at T_3.

Figure 3 shows a set of top and cross-sectional FEG-SEM images of a representative MS–NAA–PC. The structure of these heterogeneous NAA–PCs features a top layer composed of three NAA gradient-index filters with varying period length (L_{TP})—distance between adjacent nanopore modulations in depth—and a bottom NAA layer as a light-emitting film. Figure 3(a) shows a top view FEG-SEM image of this NAA–PC structure, which features hexagonally arranged, homogeneously distributed nanopores across its surface. The average nanopore diameter estimated from FEG-SEM image analysis was 17 ± 4 nm, while the interpore distance—distance between the center of adjacent nanopores—was measured to be 62 ± 5 nm. Figure 3(b) shows a general cross-sectional view FEG-SEM image of these NAA–PCs from which it is possible to discern two main layers: (i) a top light-filtering layer formed by three NAA gradient index filters labeled NAA–PC–A ($T_1 = 125$ s), NAA–PC–B ($T_2 = 150$ s), and NAA–PC–C ($T_3 = 175$ s), which feature the modulated nanopore diameter in depth; and (ii) a bottom light-emitting layer featuring straight cylindrical nanopores at the bottom labeled NAA–Ox. The thicknesses of the top and bottom layers measured by FEG-SEM image analysis were 58 ± 1 and 50 ± 1 μm, respectively. Figure 3(b) shows a set of magnified cross-sectional views showing details of nanopores at specific positions of the top and bottom layers of the MS–NAA–PC structure. FEG-SEM images of the NAA gradient-index filters forming the top light-filtering layer reveal nanopore modulations, the period length (L_{TP}) of which increases with the input anodization period (T_i). Analysis of this geometric parameter for NAA–PC–A, NAA–PC–B, and NAA–PC–C reveals that L_{TP} increases linearly with T_i at a rate of 2.1 ± 0.1 nm s^{-1}, having values of 210 ± 4, 265 ± 6, and 313 ± 8 nm for T_1, T_2, and T_3, respectively. Figure 3(c) also shows a magnified cross-sectional view of the light-emitting layer at the bottom of the MS–NAA–PC structure, which was fabricated in 0.3M oxalic acid electrolyte at 40 V for a total of ~16 h. This layer features straight cylindrical nanopores with a constant diameter from the top to the bottom. A set of FEG-SEM images of this film from a control NAA–Ox sample used to characterize the bulk PL emission of this layer are shown in Fig. S1 of the supplementary material. The 50 μm-thick layer features straight cylindrical nanopores with an average diameter of 40 ± 3 nm and an interpore distance of 101 ± 6 nm.

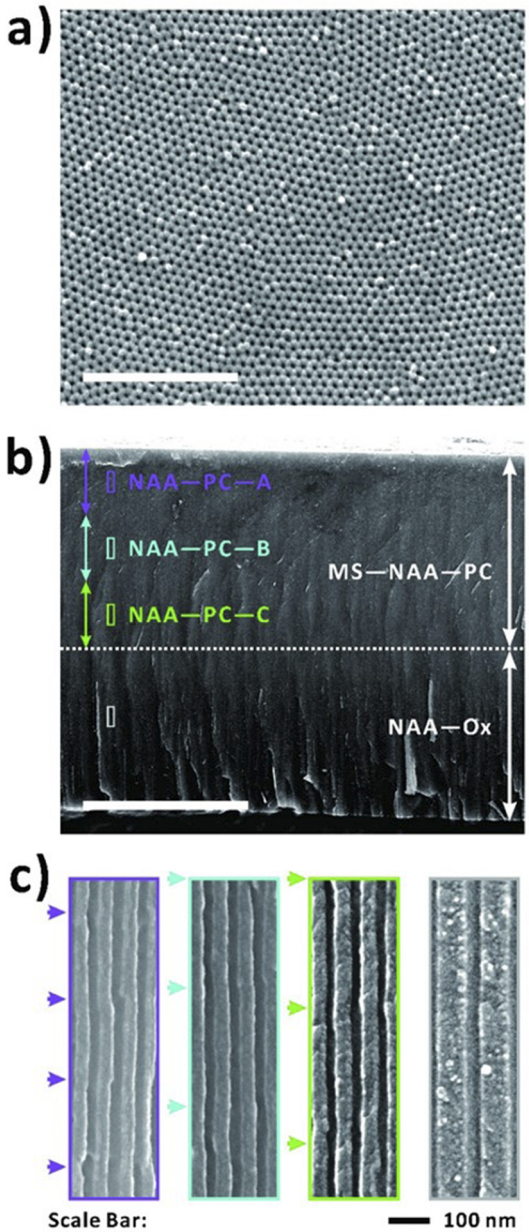

FIG. 3. Structural characterization of MS–NAA–PCs. (a) Top view FEG-SEM image of a representative MS–NAA–PC featuring an average nanopore diameter and an interpore distance of 17 ± 4 and 62 ± 5 nm, respectively (scale bar = 1 μm). (b) Full-view cross-sectional FEG-SEM image of a MS–NAA–PC featuring a light-filtering layer at its top and a light-emitting layer at its bottom with the thicknesses of 58 ± 1 mm and 50 ± 1 μm, respectively; NAA–PC–A, NAA–PC–B, and NAA–PC–C denote NAA gradient-index filters produced with $T_1 = 125$ s, $T_2 = 150$ s, and $T_3 = 175$ s, respectively; and NAA–Ox corresponds to the light-emitting layer at the bottom of the NAA–PC structures (scale bar = 50 μm). (c) Magnified view cross-sectional FEG-SEM images of color rectangles shown in (b) showing details of nanopore diameter modulations in NAA–PC–A, NAA–PC–B, and NAA–PC–C and straight cylindrical nanopores in the NAA–Ox layer (NB: color arrows denote nanopore modulations).

B. Optical characterization of MS-NAA-PCs

MS–NAA–PCs can be optically described as heterogeneous PC structures with a spectroscopic signature that results from the multiple contributions of the NAA-based gradient-index filters composing their structure (i.e., NAA–PC–A, NAA–PC–B, and

NAA–PC–C). As such, the reflection spectrum of MS–NAA–PCs features three well-resolved, intense PSBs, the features of which are critically determined by the structural features of each NAA gradient-index filter engineered by the input current density profile. The light-filtering layer on the top side of MS–NAA–PCs filters the photon-stimulated PL emission from the light-emitting layer at the bottom side of the MS–NAA–PC structure. Therefore, it is critical to characterize and understand the angle-dependence of both light reflection and light emission at the light-filtering and light-emitting layers of the MS–NAA–PC structure, respectively.

C. Effect of the incidence angle on the PSBs of MS–NAA–PCs

The effect of the incidence or excitation angle (θ) on the optical features of the PSBs of MS–NAA–PCs was systematically evaluated by reflection spectroscopy [see Fig. 4(a)]. Figure 4(b) shows the reflection spectra of MS–NAA–PCs at different incidence angles (i.e., 8°, 10°, 15° 20°, 25°, 30°, 35°, 40°, 45°, 50°, 55°, 60°, and 65°). Table S1 of the supplementary material summarizes the optical features of the three characteristic PSBs of NAA–PC–A, NAA–PC–B, and NAA–PC–C labeled PSB_1, PSB_2, and PSB_3, respectively. These include the central wavelength position (λ_{PSB}), reflection intensity (R_{PSB}), and full width at half maximum ($FWHM_{PSB}$), all estimated from Gaussian fittings. The position of the three PSBs in the reflection spectrum of MS–NAA–PCs blue shifts, while their intensity decreases with increasing angle of incidence. This result is in good agreement with the Bragg–Snell law in which the wavelength of the diffracted light depends on the angle of incidence, the periodicity, and the effective refractive index[61–63] of the nanoporous PC as expressed in the following equation:

$$m\lambda_{PSB} = 2L_{TP}\sqrt{n_{eff}^2 - sin^2\theta}, \quad (2)$$

where λ_{PSB} is the central wavelength of the PSB, m is the order of the PSB, L_{TP} is the structure periodicity, θ is the angle of incidence, and n_{eff} is the effective refractive index. Analysis of this dependence, summarized in Fig. 4(c), shows that λ_{PSB} is blue shifted at rates of -1.22 ± 0.04, -1.49 ± 0.05, and -1.78 ± 0.06 nm deg^{-1} for PSB_1, PSB_2, and PSB_3, respectively. Fig. S2 of the supplementary material shows the dependence of R_{PSB} and $FWHM_{PSB}$ as a function of the incidence angle, which indicates that the reflection intensity of the PSB decreases with increasing angle of incidence. Analysis of the fitting lines shown in Fig. S2a of the supplementary material denotes that R_{PSB} decreases at rates of -0.37 ± 0.02, -0.39 ± 0.007, and -0.38 ± 0.016 a.u. deg^{-1} for PSB_1, PSB_2, and PSB_3, respectively. It is apparent from Fig. S2b of the supplementary material that the dependence of $FWHM_{PSB}$ with the angle of incidence follows a Gaussian-like trend, where this optical feature increases until 40° and dramatically decreases from >45° to 65°. Trends for $FWHM_{PSB}$'s PSB_1, PSB_2, and PSB_3 were determined to be $FWHM_1 = 7.53 + ((64.63)/(34.64 \cdot p/2) \cdot Exp(-2 \cdot (\theta - 36.59/(34.65))$, $FWHM_2 = -4.74 + ((2363.2)/(123.63 \cdot p/2) \cdot Exp(-2 \cdot (\theta - 33.84/(123.63))$, and $FWHM_3 = 9.19 + ((125.62)/(33.0 \cdot p/2) \cdot Exp(-2 \cdot (\theta - 35.92/(33.0))$ from Gaussian fittings, respectively.

D. Effect of the incidence angle on the PL of the light-emitting layer in MS–NAA–PCs

Photoluminescence of NAA is attributable to oxygen vacancies distributed across the onion-like composition of anodic alumina and oxalic impurities incorporated into its structure from the acid electrolyte during the anodization process. Of all types, NAA produced in oxalic acid electrolyte has the highest PL emission.[49–51] Conversely, the characteristic PL emission from NAA produced in sulfuric acid electrolyte is weak and almost negligible to that of NAA structures produced in oxalic acid electrolyte. For this reason,

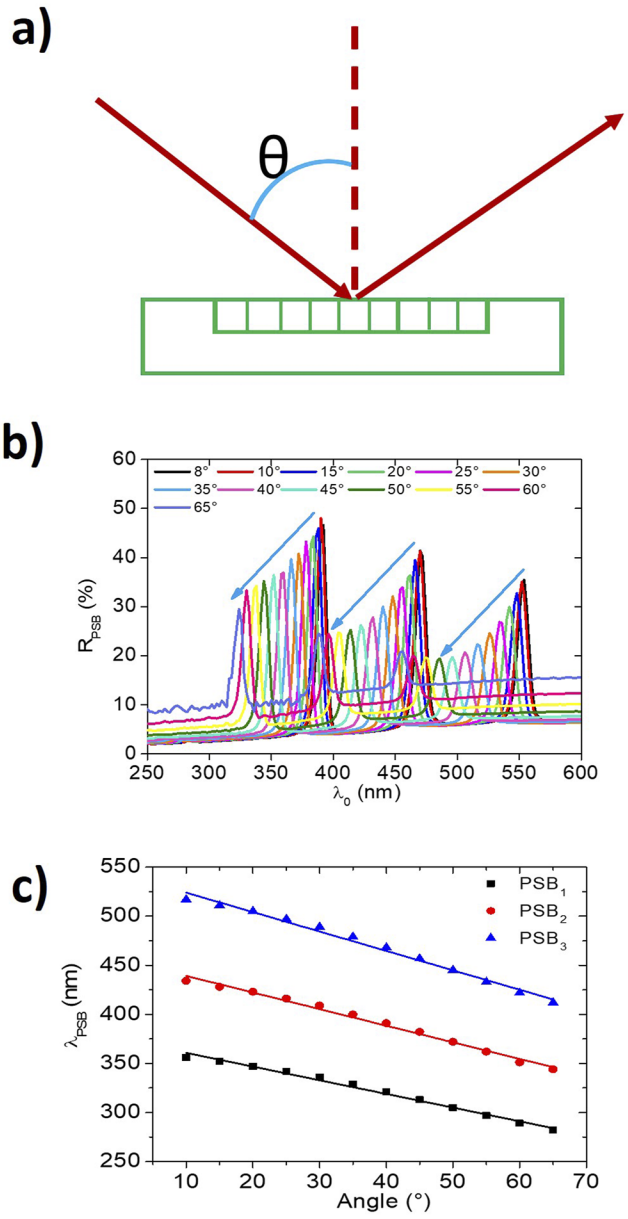

FIG. 4. Effect of the incidence angle on the optical features of the PSBs of MS–NAA–PCs. (a) Schematic showing the variation in the incidence angle. (b) Reflection spectra of a representative MS–NAA–PC as a function of the angle of incidence, from $\theta = 8°$ to 65°. (c) Central wavelength position of MS–NAA–PC's PSB_1, PSB_2, and PSB_3 (λ_{PSB}) as a function of θ.

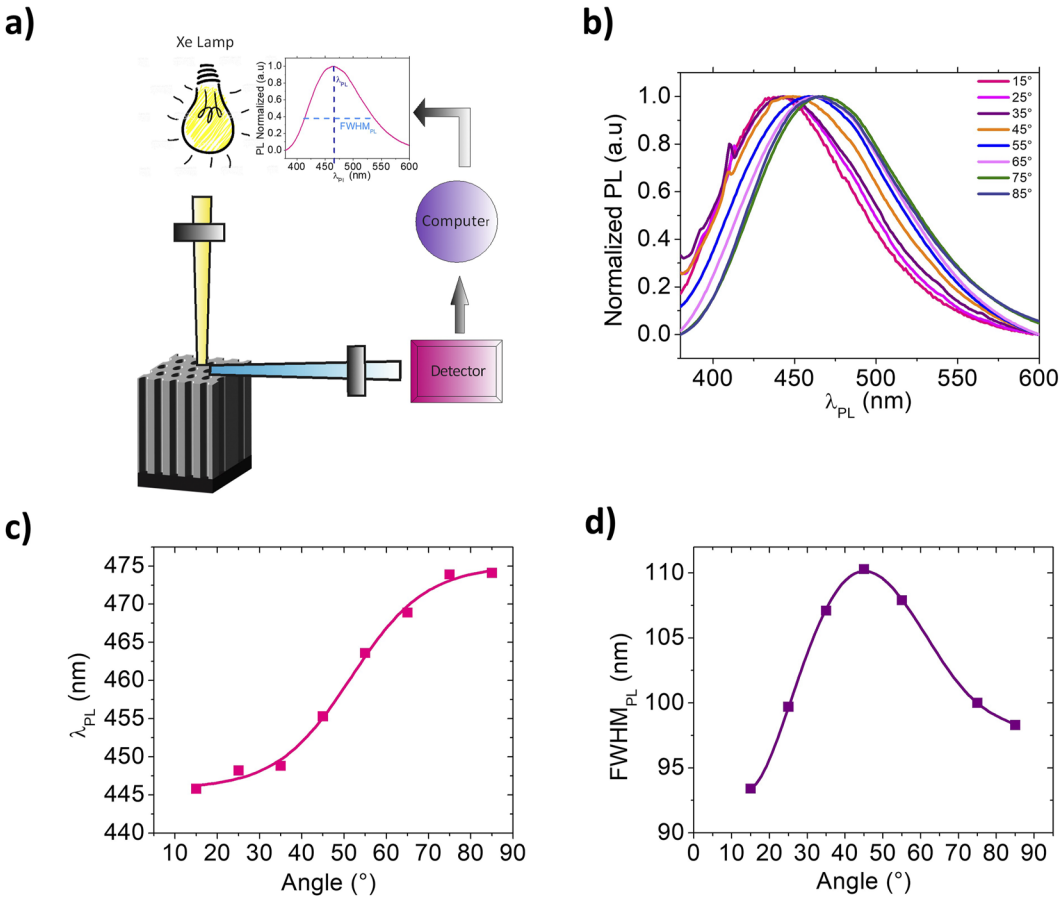

FIG. 5. Photoluminescent emission from NAA films. (a) Schematic illustration of the PL setup used to characterize PL emission from MS–NAA–PCs and NAA–Ox films. (b) Characteristic Gaussian-like PL emission at varying angle of incidence from 15° to 85° from a reference NAA–Ox film fabricated in oxalic acid electrolyte by two step anodization (NB: λ_{ex} = 350 nm). (c) Dependence of the central wavelength position of PL emission (λ_{PL}) with the angle of incidence. (d) Dependence of full width at half maximum of PL emission ($FWHM_{PL}$) with the angle of incidence.

we devised the structure of MS–NAA–PCs featuring a top light-filtering layer having an almost negligible PL emission and a bottom light-emitting layer with strong PL emission. Figure 5(a) shows a schematic illustration of the experimental setup used to characterize PL emissions from MS–NAA–PCs. Figure 5(b) shows the characteristic PL emission at different angles of incidence from 15° to 85° with an interval of 10° from a representative 50 μm-thick NAA film fabricated by two-step anodization in oxalic acid electrolyte. The emission spectrum of the NAA film is characterized by a broad, intense, Gaussian-like emission band across the 380–600 nm range for all the angles of incidence analyzed. It is apparent from Fig. 5(c) that the position of the PL band (λ_{PL}) is shifted toward longer wavelengths (i.e., red shift) with increasing angle of incidence, following a sigmoidal trend where $\lambda_{PL} = 475.04 + (445.8 - 475.04)/1 + \text{Exp}(\theta - 51.67/8.82)$. This graph indicates a slight red shift of λ_{PL} with θ from 445 nm at 15° to 448 nm at 35°. However, λ_{PL} undergoes a significant shift between 35° and 75°, in which λ_{PL} red shifts its position from 448 to 479 nm, respectively, and it stabilizes its position for $\theta > 75°$. Figure 5(d) shows the dependence of $FWHM_{PL}$ with the angle of incidence. It is apparent that $FWHM_{PL}$ follows a Gaussian-like trend with θ, where this optical feature initially increases with angle of incidence until 45°. At this angle, $FWHM_{PL}$ achieves its maximum value of 115 ± 1 nm. For $\theta > 45°$, $FWHM_{PL}$ starts to decrease until a minimum of 98 ± 2 nm at an angle of 85°. Table S2 of the supplementary material summarizes the dependence of λ_{PL} and $FWHM_{PL}$ with the angle of incidence for a representative light-emitting NAA film produced in oxalic acid electrolyte.

E. Photoluminescence of MS–NAA–PCs

MS–NAA–PCs were fabricated to feature three well-resolved PSBs at specific spectral positions within the PL emission of NAA–Ox films (i.e., ~400–600 nm). To this end, the structure of MS–NAA–PCs was judiciously engineered with three stacked gradient-index filters embedded within the same heterogeneous PC structure. These heterogeneous NAA-based PCs were used as

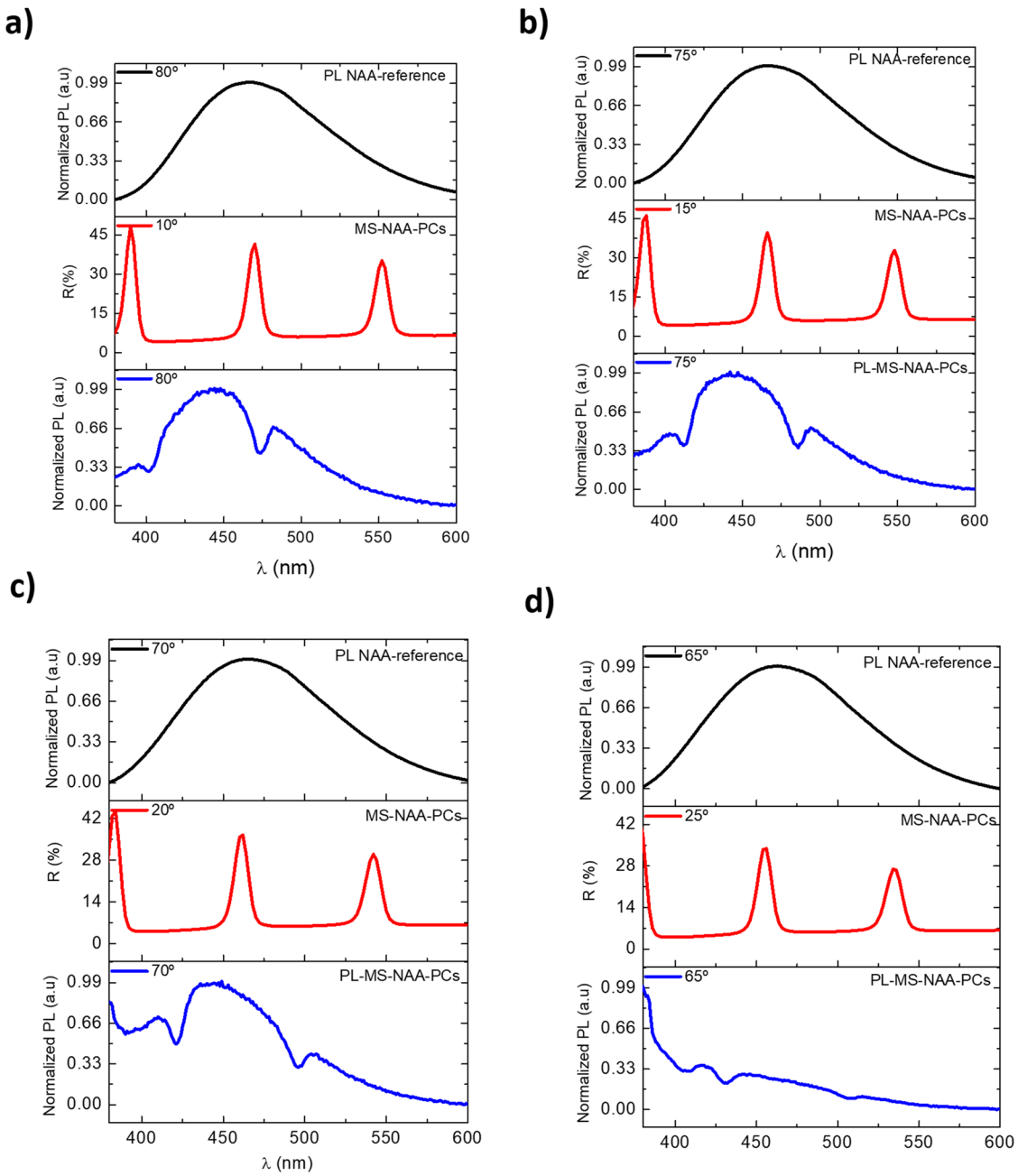

FIG. 6. Photoluminescence emission of MS–NAA–PC with PL spectra of NAA of oxalic acid as a reference (black line), reflection spectra of MS–NAA–PC (red line), and PL spectra of MS–NAA–PC (blue line) at: (a) 10° (reflection) and 80° (PL emission), (b) 15° (reflection) and 75° (PL emission), (c) 20° (reflection) and 70° (PL emission), and (d) 25° (reflection) and 65° (PL emission) (NB: angles of reflection and emission were complementary at $25° - \theta_{reflection} + \theta_{emission} = 90°$).

model platforms to study for the first time the light-filtering properties of NAA–PCs, harnessing the intrinsic light-emitting properties of NAA. MS–NAA–PCs were mounted on a rotating stage, which allows the PL signal to be measured at different angles of excitation and emission. Excitation light at 355 nm was shone onto the center of MS–NAA–PCs and the emission was collected from 380 to 600 nm at varying angle of incidence. Figure 6 shows the PL emission of a reference NAA–Ox film (black line), the reflection (red line) spectrum, and PL emission (blue line) of MS–NAA–PCs at varying angle of incidence (i.e., 65°, 70°, 75°, and 80° for PL

and complementary reflection angles of 25°, 20°, 15°, and 10° for reflection). It is apparent that the generation of three gradient-index filters on top of the light-emitting NAA–Ox layer filters efficiently the PL emission from the NAA–Ox layer by narrowing $FWHM_{PL}$ and shifting λ_{PL} following an angle-dependent pattern. $FWHM_{PL}$ of the PL emission of the NAA–Ox film at 80°, 75°, 70°, and 65° was measured to be 99 ± 2, 100 ± 2, 103 ± 1, and 105 ± 1 nm, respectively [see Figs. 6(a)–6(d)]. Upon generation of MS–NAA–PCs on top of the light-emitting NAA–Ox layer, $FWHM_{PL}$ is narrowed to 93 ± 2, 88 ± 2, 97 ± 3, and 88 ± 6 nm at 80°, 75°, 70°, and 65°, respectively. This result indicates that light emission is filtered by the top gradient-index filters. It is also found that λ_{PL} red shifts its position with decreasing angle of incidence, having values of 443 ± 1, 447 ± 1, 451 ± 1, and 450 ± 1 nm at 80°, 75°, 70°, and 65°, respectively [see Figs. 6(a)–6(d)]. For instance, the PL emission of MS–NAA–PCs at 80° [see Fig. 6(a)] shows two local minima or shoulders at 402 and 473 nm, which would correspond to light-emitting inhibition associated with PSB_1 (389 nm) and PSB_2 (461 nm), respectively. At that angle of incidence, PSB_3 (551 nm) is far from the main Gaussian-like PL emission. Therefore, it is inferred that this gradient-index filter does not contribute to the filtered PL emission from the MS–NAA–PC structure within this spectral region. Upon reduction in the angle of incidence, the characteristic PBSs of the MS–NAA–PC structure undergo a blue shift, which, in turn, changes the characteristics of the light beam emitted from the underlying NAA–Ox film. Figure 6(b) shows that the local minima of the PL emission from MS–NAA–PCs at 75° feature two local minima at 412 and 486 nm, which would correspond to light-emitting inhibition associated with PSB_1 (387 nm) and PSB_2 (466 nm), respectively. At that angle of incidence, PSB_3 is located at 548 nm, which is still far from the spectral position of the PL emission and does not contribute significantly to filtering. Figure 6(c) shows that the local minima of the PL emission of MS–NAA–PCs at 70° feature two local minima at 421 and 497 nm, which would correspond to light-emitting inhibition associated with PSB_1 (382 nm) and PSB_2 (466 nm), respectively. At that angle of incidence, PSB_3 is located at 541 nm, which is still far from the spectral position of the PL emission and does not contribute significantly to filtering. Figure 6(d) shows that the local minima of the PL emission of MS–NAA–PCs at 65° feature two local minima at 430 and 507 nm, which would correspond to light-emitting inhibition associated with PSB_1 (377 nm) and PSB_2 (455 nm), respectively. At that angle of incidence, PSB_3 is located at 541 nm, which is still far from the spectral position of the PL emission and does not contribute significantly to PL emission filtering. The optical properties of MS-NAA-PCs were modeled by combining an effective medium approximation (EMA) model and the transfer matrix method (TMM). The effective refractive index of each layer within MS–NAA–PCs' structure was estimated by the Looyenga–Landau–Lifshitz (3L) EMA model. Figure S3 of the supplementary material shows a comparison between experimental and simulation data. These data demonstrate that simulations can predict the spectral position (λ) and the reflection (R) of the PSB of MS–NAA–PCs with excellent accuracy with a deviation of 0.68% (λ) for the spectral position and 1.7% for the reflection (%R).

To gain further insight into the light-filtering properties of MS–NAA–PCs and the dependence of PL emission, we analyzed the optical features of PL emission at distinct angle of incidence. At first glance, Fig. 7(a) reveals an interesting effect where light emitted from

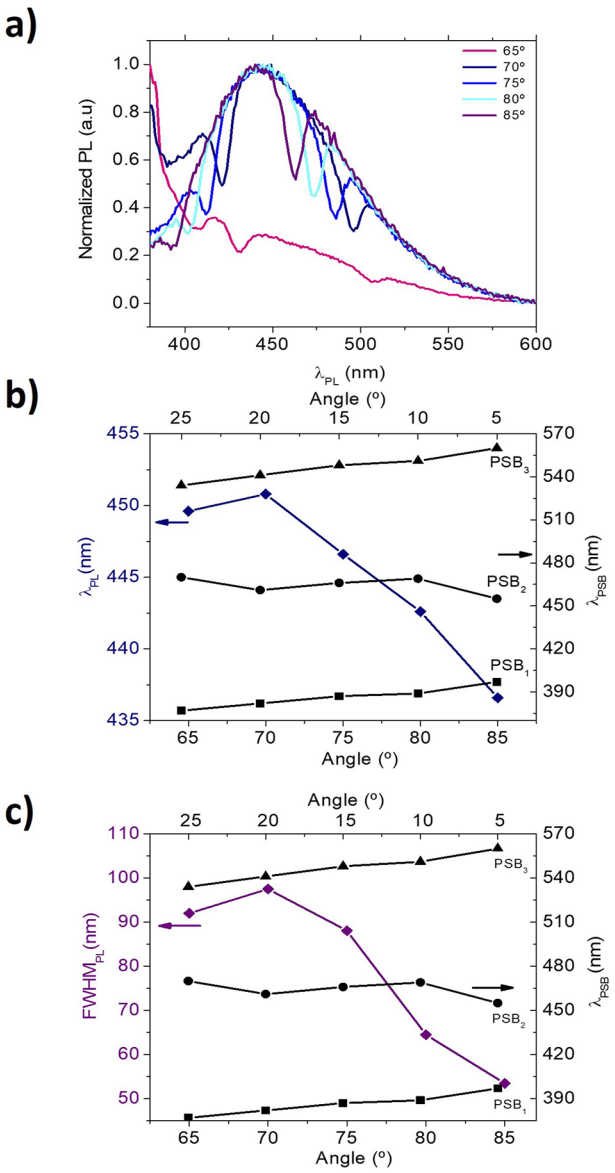

FIG. 7. Summary of the position of PSB_1, PSB_2, and PSB_3 and the features of PL emission from MS–NAA–PCs (NB: angles of reflection and emission were complementary at 25° − θ reflection + θ emission = 90°). (a) PL emission from MS–NAA–PCs at 65°, 70°, 75°, 80°, and 85°. (b) Dependence of λ_{PL} and the position of PSB_1, PSB_2, and PSB_3 in MS–NAA–PCs with the angle of incidence. (c) Dependence of $FWHM_{PL}$ and the position of PSB_1, PSB_2 and PSB_3 in MS–NAA–PCs with the angle of incidence.

the underlying photoluminescent layer is narrowed and shifted with the angle of incidence. Figures 7(b) and 7(c) summarize the positions of the characteristic PSB_1, PSB_2, and PSB_3 and the features of the PL emission ($FWHM_{PL}$ and λ_{PL}) from MS–NAA–PCs. It is apparent that the position of PL emission (λ_{PL}) undergoes a slight red shift when the angle of incidence is increased from 65° to 70°

(i.e., from 450 to 451 nm, respectively) [see Fig. 7(b)]. After this point, the light-filtering layer of MS–NAA–PCs blue shifts the position of the Gaussian-like PL emission from the light-emitting NAA–Ox layer at the bottom of the heterogeneous NAA–PC structure. PL emission from 70° to 85° is found to blue shift linearly from 451 to 437 nm at a rate of −0.93 nm deg^{-1}. Dependence of $FWHM_{PL}$ with the angle of incidence is found to follow a qualitatively similar trend. Initially, PL emission is slightly widened from 65° to 70°, where this optical feature increases from 92 to 97 nm, respectively [see Fig. 7(c)]. However, the light-filtering layer of MS–NAA–PCs can efficiently narrow PL emission from 70° to 85°, where $FWHM_{PL}$ is found to be sharply and linearly narrowed from 97 to 54 nm at a rate of −3.11 nm deg^{-1}. These results clearly demonstrate that the structural design of NAA–PCs can be judiciously harnessed to tune and control the features of the intrinsic photoluminescence emission of this highly tailorable platform material. NAA is a platform material that offers unique properties, such as chemical, mechanical, and thermal stability, under different conditions. As such, light-emitting NAA-based PC structures are an alternative platform for other porous materials, such as porous silicon, which is limited by its low chemical stability without additional passivation steps and its fragile mechanical strength. Consequently, our findings provide new opportunities to develop NAA-based optical systems for a broad range of photonic technologies. It is also worth noting that the intrinsic properties of NAA can be further modified to modulate its light-emitting properties. Recent studies have demonstrated that doping with rare earths enables strong enhancement of the intrinsic electroluminescence of this material, paving the way for new light-emitting devices and systems.[64,65]

IV. CONCLUSIONS

To the best of our knowledge, this study is the first demonstration of structural tuning of intrinsic photoluminescence emissions from nanoporous anodic alumina photonic crystals. We have harnessed a smart structural design in which a non-emitting, light-filtering layer in the form of multi-spectral NAA–PC is combined with an intrinsically light-emitting layer of NAA. MS–NAA–PCs feature three intense, well-resolved photonic stopbands, the positions of which can be spaced across the visible spectrum from ~380 to 560 nm. This approach makes it possible to engineer the three photonic stopbands in the top light-filtering layer to effectively narrow and tune photoluminescence emission from the underlying light-emitting layer. Alignment of the PSBs makes it possible to narrow the width of its photoluminescence emission up to ~50 nm and blue shift its position for ~15 nm. Inhibition of light emission is accomplished by harnessing forbidden light propagation through the characteristic photonic stopbands of the top light-filtering layer. MS–NAA–PCs enable control over intrinsic photoluminescence of NAA without the use of external PL emitters, such as dyes and fluorophores. Our findings provide exciting new opportunities to engineer the intrinsic light-emitting properties of NAA-based photonic crystals structures, which have implications across a variety of photonic technologies, such as sensing and biosensing, lasing and light sources, photodetection, photocatalysis, green energy generation, and solar light harvesting.

SUPPLEMENTARY MATERIAL

See the supplementary material for the structural characterization of NAA films, effect of the incidence angle on the optical features of MS-NAA-PCs, and summary of the optical features of NAA and MS-NAA PCs.

ACKNOWLEDGMENTS

This work was supported by the Spanish Ministerio de Ciencia, Innovación y Universidades (MICINN/FEDER) (Grant No. RTI2018-094040-B-I00) and by the Agency for Management of University and Research Grants (AGAUR) (Reference No. 2017-SGR-1527). The authors acknowledge the support provided by the Australian Research Council under Grant Nos. CE140100003 and DP200102614, the School of Chemical Engineering, The University of Adelaide, the Institute for Photonics and Advanced Sensing, and the ARC Centre of Excellence for Nanoscale BioPhotonics.

AUTHOR DECLARATIONS

Conflict of Interest

The authors have no conflicts to disclose.

Author Contributions

Dr. L.K.A. and Dr. C.S.L. carried out the experimental part. Professor L.F.M. conceived the idea and designed the experimental part of this work in collaboration with Dr. A.S. and Dr. J.F.-B. The obtained results were discussed and analyzed by all the authors. The manuscript was written through contributions of all authors. All authors have given approval to the final version of the manuscript.

DATA AVAILABILITY

The data that support the findings of this study are available from the corresponding author upon reasonable request.

REFERENCES

[1] C. Parker, "Photoluminescence of solutions with applications to photochemistry and analitycal chemistry," Nature **220**, 1968 (1968).
[2] X. Sun, F. Xu, Z. Li, and W. Zhang, "Photoluminescence properties of anodic alumina membranes with ordered nanopore arrays," J. Lumin. **121**(2), 588–594 (2006).
[3] H. Wang, K. Ferrio, D. G. Steel, Y. Z. Hu, R. Binder, and S. W. Koch, "Transient nonlinear optical response from excitation induced dephasing in GaAs," Phys. Rev. Lett. **71**(8), 1261–1264 (1993).
[4] M. N. Shkunov, Z. V. Vardeny, M. C. DeLong, R. C. Polson, A. A. Zakhidov, and R. H. Baughman, "Tunable, gap-state lasing in switchable directions for opal photonic crystals," Adv. Funct. Mater. **12**(1), 21–26 (2002).
[5] V. L. Colvin, M. C. Sclamp, and A. P. Allvisatos, "Light-emitting diodes made from cadmium selenide nanocrystals and a semiconducting polymer," Nature **370**, 354 (1994).
[6] J. Lim, S. Jun, E. Jang, H. Baik, H. Kim, and J. Cho, "Preparation of highly luminescent nanocrystals and their application to light-emitting diodes," Adv. Mater. **19**(15), 1927–1932 (2007).
[7] J. K. Jaiswal and S. M. Simon, "Potentials and pitfalls of fluorescent quantum dots for biological imaging," Trends Cell Biol. **14**(9), 497–504 (2004).
[8] W. C. W. Chan, D. J. Maxwell, X. Gao, R. E. Bailey, M. Han, and S. Nie, "Luminescent quantum dots for multiplexed biological detection and imaging," Curr. Opin. Biotechnol. **13**(1), 40–46 (2002).

[9]Y. Zhang, J. Qiu, M. Gao, P. Li, L. Gao, L. Heng, B. Z. Tang, and L. Jiang, "A visual film sensor based on silole-infiltrated SiO_2 inverse opal photonic crystal for detecting organic vapors," J. Mater. Chem. C **2**(42), 8865–8872 (2014).
[10]A. C. Arsenault, T. J. Clark, G. Von Freymann, L. Cademartiri, R. Sapienza, J. Bertolotti, E. Vekris, S. Wong, V. Kitaev, I. Manners *et al.*, "From colour fingerprinting to the control of photoluminescence in elastic photonic crystals," Nat. Mater. **5**(3), 179–184 (2006).
[11]K. Aoki, D. Guimard, M. Nishioka, M. Nomura, S. Iwamoto, and Y. Arakawa, "Coupling of quantum-dot light emission with a three-dimensional photonic-crystal nanocavity," Nat. Photonics **2**(11), 688–692 (2008).
[12]A. Santos, "Nanoporous anodic alumina photonic crystals: Fundamentals, developments and perspectives," J. Mater. Chem. C **5**(23), 5581–5599 (2017).
[13]A. Santos, C. S. Law, T. Pereira, and D. Losic, "Nanoporous hard data: Optical encoding of information within nanoporous anodic alumina photonic crystals," Nanoscale **8**(15), 8091–8100 (2016).
[14]T. Kumeria, A. Santos, M. M. Rahman, J. Ferré-Borrull, L. F. Marsal, and D. Losic, "Advanced structural engineering of nanoporous photonic structures: Tailoring nanopore architecture to enhance sensing properties," ACS Photonics **1**, 1298–1306 (2014).
[15]D. Biallo, A. D'Orazio, M. De Sario, V. Marrocco, V. Petruzzelli, and F. Prudenzano, "Photonic crystal sensors," in *2006 International Conference on Transparent Optical Networks* (IEEE, 2006), Vol. 2, pp. 44–48.
[16]G. Macias, J. Ferré-Borrull, J. Pallarès, and L. F. Marsal, "1-D nanoporous anodic alumina rugate filters by means of small current variations for real-time sensing applications," Nanoscale Res. Lett. **9**(1), 315 (2014).
[17]C. S. Law, S. Y. Lim, A. D. Abell, N. H. Voelcker, and A. Santos, "Nanoporous anodic alumina photonic crystals for optical chemo- and biosensing: Fundamentals, advances, and perspectives," Nanomaterials **8**(10), 788 (2018).
[18]A. Santos, T. Pereira, C. S. Law, and D. Losic, Nanoscale **8**, 14846–14857 (2016).
[19]S. W. Chen, T. C. Lu, Y. J. Hou, T. C. Liu, H. C. Kuo, and S. C. Wang, "Lasing characteristics at different band edges in GaN photonic crystal surface emitting lasers," Appl. Phys. Lett. **96**(7), 071108 (2010).
[20]Y. Fu and T. Zhai, "Distributed feedback organic lasing in photonic crystals," Front. Optoelectron. **13**, 18 (2019).
[21]M. Notomi, H. Suzuki, and T. Tamamura, "Directional lasing oscillation of two-dimensional organic photonic crystal lasers at several photonic band gaps," Appl. Phys. Lett. **78**(10), 1325–1327 (2001).
[22]S. Azzini, D. Gerace, M. Galli, I. Sagnes, R. Braive, A. Lemaître, J. Bloch, and D. Bajoni, "Ultra-low threshold polariton lasing in photonic crystal cavities," Appl. Phys. Lett. **99**(11), 111106 (2011).
[23]W. Yang, B. Wang, A. Sun, J. Liu, and G. Xu, "Lasing from dye-loaded periodic anodic alumina nanostructure," Mater. Lett. **178**, 197–200 (2016).
[24]H. Masuda, M. Yamada, F. Matsumoto, S. Yokoyama, S. Mashiko, M. Nakao, and K. Nishio, "Lasing from two-dimensional photonic crystals using anodic porous alumina," Adv. Mater. **18**(2), 213–216 (2010).
[25]S. Y. Lim, C. S. Law, M. Markovic, J. K. Kirby, A. D. Abell, and A. Santos, "Engineering the slow photon effect in photoactive nanoporous anodic alumina gradient-index filters for photocatalysis," ACS Appl. Mater. Interfaces **10**(28), 24124–24136 (2018).
[26]L. Liu, S. Y. Lim, C. S. Law, B. Jin, A. D. Abell, G. Ni, and A. Santos, "Light-confining semiconductor nanoporous anodic alumina optical microcavities for photocatalysis," J. Mater. Chem. A **7**(39), 22514–22529 (2019).
[27]M. Barth, A. Gruber, and F. Cichos, "Spectral and angular redistribution of photoluminescence near a photonic stop band," Phys. Rev. B **72**(8), 085129 (2005).
[28]R. C. Schroden, M. Al-Daous, and A. Stein, "Self-modification of spontaneous emission by inverse opal silica photonic crystals," Chem. Mater. **13**(9), 2945–2950 (2001).
[29]H. Masuda and K. Fukuda, "Ordered metal nanohole arrays made by two-step replication of honeycomb structures of anodic alumina," Science **268**(5216), 1466–1468 (1995).
[30]J. Ferré-Borrull, J. Pallarès, G. Macías, and L. F. Marsal, "Nanostructural engineering of nanoporous anodic alumina for biosensing applications," Materials **7**(7), 5225–5253 (2014).
[31]W. Lee and J. C. Kim, "Highly ordered porous alumina with tailor-made pore structures fabricated by pulse anodization," Nanotechnology **21**(48), 485304 (2010).
[32]M. Pashchanka and J. J. Schneider, "Self-ordering regimes of porous anodic alumina layers formed in highly diluted sulfuric acid electrolytes," J. Phys. Chem. C **120**(27), 14590–14596 (2016).
[33]L. P. Hernández-Eguía, J. Ferré-Borrull, G. Macias, J. Pallarès, and L. F. Marsal, "Engineering optical properties of gold-coated nanoporous anodic alumina for biosensing," Nanoscale Res. Lett. **9**(1), 414 (2014).
[34]G. D. Sulka, in *Highly Ordered Anodic Porous Alumina Formation by Self-Organized Anodizing*, 1st ed., edited by A. Eftekhari (Wiley-VCH Verlag GmbH & Co., Weinheim, 2008).
[35]S. Shingubara, "Fabrication of nanomaterials using porous alumina templates," J. Nanopart. Res. **5**(1), 17–30 (2003).
[36]L. F. Marsal, L. Vojkuvka, P. Formentin, J. Pallarés, and J. Ferré-Borrull, "Fabrication and optical characterization of nanoporous alumina films annealed at different temperatures," Opt. Mater. **31**(6), 860–864 (2009).
[37]Y. Li, G. H. L. Li, G. W. Meng, and L D. Zhang, "Photoluminescence and optical absorption caused by the F+ centres in anodic alumina membranes," J. Phys.: Condens. Matter **13**(11), 2691–2699 (2001).
[38]G. S. Huang, X. L. Wu, Y. F. Mei, X. F. Shao, and G. G. Siu, "Strong blue emission from anodic alumina membranes with ordered nanopore array," J. Appl. Phys. **93**(1), 582–585 (2003).
[39]G. S. Huang, X. L. Wu, L. W. Yang, X. F. Shao, G. G. Siu, and P. K. Chu, "Dependence of blue-emitting property on nanopore geometrical structure in Al-based porous anodic alumina membranes," Appl. Phys. A **81**(7), 1345–1349 (2005).
[40]N. I. Mukhurov, S. P. Zhvavyi, I. V. Gasenkova, S. N. Terekhov, P. P. Pershukevich, and V. A. Orlovich, "Photoluminescence of f-centres in films of anodic alumina," J. Appl. Spectrosc. **77**(4), 549 (2010).
[41]Y. Du, W. L. Cai, C. M. Mo, J. Chen, L. D. Zhang, and X. G. Zhu, "Preparation and photoluminescence of alumina membranes with ordered pore arrays," Appl. Phys. Lett. **74**(20), 2951–2953 (1999).
[42]A. Rauf, M. Mehmood, M. Ahmed, M. ul Hasan, and M. Aslam, "Effects of ordering quality of the pores on the photoluminescence of porous anodic alumina prepared in oxalic acid," J. Lumin. **130**(5), 792–800 (2010).
[43]G. S. Huang, X. L. Wu, G. G. Siu, and P. K. Chu, "On the origin of light emission from porous anodic alumina formed in sulfuric acid," Solid State Commun. **137**(11), 621–624 (2006).
[44]A. Nourmohammadi, S. J. Asadabadi, M. H. Yousefi, and M. Ghasemzadeh, "Photoluminescence emission of nanoporous anodic aluminum oxide films prepared in phosphoric acid," Nanoscale Res. Lett. **7**(1), 689 (2012).
[45]I. Vrublevsky, K. Chernyakova, A. Ispas, A. Bund, N. Gaponik, and A. Dubavik, "Photoluminescence properties of heat-treated porous alumina films formed in oxalic acid," J. Lumin. **131**(5), 938–942 (2011).
[46]Y.-F. Liu, Y.-F. Tu, S.-Y. Huang, J.-P. Sang, and X.-W. Zou, "Effect of etch-treatment upon the intensity and peak position of photoluminescence spectra for anodic alumina films with ordered nanopore array," J. Mater. Sci. **44**, 3370–3375 (2009).
[47]A. Santos, M. Alba, M. M. Rahman, P. Formentin, J. Ferre-Borrull, J. Pallares, and L. F. Marsal, "Structural tuning of photoluminescence in nanoporous anodic alumina by hard anodization in oxalic and malonic acids," Nanoscale Res. Lett. **7**(1), 228 (2012).
[48]P. R. Reddy, K. M. Ajith, and N. K. Udayashankar, "Morphological analysis and photoluminescence properties of hydrophilic porous anodic alumina formed in oxalic acid," J. Mater. Sci.: Mater. Electron. **27**(5), 5331–5344 (2016).
[49]N. I. Mukhurov, S. P. Zhvavyi, S. N. Terekhov, A. Yu. Panarin, I. F. Kotova, P. P. Pershukevich *et al.*, "Influence of electrolyte composition on photoluminescent properties of anodic aluminum oxide," J. Appl. Spectrosc. **75**(2), 214–218 (2008).
[50]W. J. Stępniowski, A. Nowak-Stępniowska, and Z. Bojar, "Quantitative arrangement analysis of anodic alumina formed by short anodizations in oxalic acid," Mater. Charact. **78**, 79 (2013).
[51]G. S. Huang, X. L. Wu, Y. Xie, X. F. Shao, and S. H. Wang, "Light emission from silicon-based porous anodic alumina formed in 0.5 M oxalic acid," J. Appl. Phys. **94**(4), 2407–2410 (2003).
[52]K. S. Choudhari, S. D. Kulkarni, C. Santosh, and S. D. George, "Influence of electrolyte composition on the photoluminescence and pore arrangement of nanoporous anodic alumina," ECS J. Solid State Sci. Technol. **7**(11), R175–R182 (2018).

[53]A. Santos, J. Ferré-Borrull, J. Pallarès, and L. F. Marsal, "Hierarchical nanoporous anodic alumina templates by asymmetric two-step anodization," Phys. Status Solidi A **208**(3), 668–674 (2011).
[54]A. Santos, P. Formentín, J. Ferré-Borrull, J. Pallarès, and L. F. Marsal, "Nanoporous anodic alumina obtained without protective oxide layer by hard anodization," Mater. Lett. **67**(1), 296–299 (2012).
[55]A. Santos, J. M. Montero-Moreno, J. Bachmann, K. Nielsch, P. Formentín, J. Ferré-Borrull, J. Pallarès, and L. F. Marsal, "Understanding pore rearrangement during mild to hard transition in bilayered porous anodic alumina membranes," ACS Appl. Mater. Interfaces **3**(6), 1925–1932 (2011).
[56]A. Santos, L. Vojkuvka, M. Alba, V. S. Balderrama, J. Ferré-Borrull, J. Pallarès, and L. F. Marsal, "Understanding and morphology control of pore modulations in nanoporous anodic alumina by discontinuous anodization," Phys. Status Solidi A **209**(10), 2045–2048 (2012).
[57]N. Hauke, T. Zabel, K. Muller, M. Kaniber, A. Laucht, D. Bougeard, G. Abstreiter, J. J. Finley, and Y. Arakawa, "Enhanced photoluminescence emission from two-dimensional silicon photonic crystal nanocavities. New J. Phys. **12**, 053005 (2010).
[58]M. Bayindir, S. Tanriseven, A. Aydinli, and E. Ozbay, "Rapid communication: Strong enhancement of spontaneous emission in amorphous-silicon-nitride photonic crystal based coupled-microcavity structures," Appl. Phys. A **73**, 125–127 (2001).
[59]L. K. Acosta, F. Bertó-Roselló, E. Xifre-Perez, A. Santos, J. Ferré-Borrull, and L. F. Marsal, "Stacked nanoporous anodic alumina gradient-index filters with tunable multispectral photonic stopbands as sensing platforms," ACS Appl. Mater. Interfaces **11**(3), 3360–3371 (2019).
[60]C. A. Schneider, W. S. Rasband, and K. W. Eliceiri, "NIH image to ImageJ: 25 years of image analysis," Nat. Methods **9**(7), 671–675 (2012).
[61]I. V. Nemtsev, I. A. Tambasov, A. A. Ivanenko, and V. Y. Zyryanov, "Angle-resolved reflection spectroscopy of high-quality PMMA opal crystal," Photonics Nanostruct.: Fundam. Appl. **28**, 37–44 (2018).
[62]L. K. Acosta, F. Berto, E. Xifre-perez, C. S. Law, A. Santos, J. Ferre, L. F. Marsal, "Tunable nanoporous anodic alumina photonic crystals by Gaussian pulse anodization," ACS Appl. Mater. Interfaces **12**, 19778 (2020).
[63]G. Mayonado, S. M. Mian, V. Robbiano, and F. Cacialli, "Investigation of the Bragg-Snell law in photonic crystals," in 2015 Conference of Laboratory Instruction Beyond the First Year of Collage (2015), pp. 60–63.
[64]T. Maeno and S. Morisaki, "Electroluminescence from barrier-type anodic oxide alumina films doped with rare-earth and transition metals by ion-implantation," Jpn. J. Appl. Phys., Part 1 **39**, 6296 (2000).
[65]W. M. De Azevedo, D. D. De Carvalho, E. A. De Vasconcelos, and E. F. Da Silva, "Photoluminescence characteristics of rare earth-doped nanoporous aluminum oxide," Appl. Surf. Sci. **234**, 457 (2004).